High-ammonia selective metal–organic framework–derived Co-doped Fe/Fe_2O_3 catalysts for electrochemical nitrate reduction

Shuo Zhang[a], Miao Li[a,1], Jiacheng Li[a], Qinan Song[a], and Xiang Liu[a]

[a]School of Environment, Tsinghua University, Beijing 100084, China

Edited by Alexis Bell, Department of Chemical and Biomolecular Engineering, University of California, Berkeley, CA; received August 23, 2021; accepted November 15, 2021

Ammonia (NH_3) is an ideal carbon-free power source in the future sustainable hydrogen economy for growing energy demand. The electrochemical nitrate reduction reaction (NO_3^-RR) is a promising approach for nitrate removal and NH_3 production at ambient conditions, but efficient electrocatalysts are lacking. Here, we present a metal–organic framework (MOF)–derived cobalt-doped Fe@Fe_2O_3 (Co-Fe@Fe_2O_3) NO_3^-RR catalyst for electrochemical energy production. This catalyst has a nitrate removal capacity of 100.8 mg N g_{cat}^{-1} h^{-1} and an ammonium selectivity of 99.0 ± 0.1%, which was the highest among all reported research. In addition, NH_3 was produced at a rate of 1,505.9 μg h^{-1} cm^{-2}, and the maximum faradaic efficiency was 85.2 ± 0.6%. Experimental and computational results reveal that the high performance of Co-Fe@Fe_2O_3 results from cobalt doping, which tunes the Fe d-band center, enabling the adsorption energies for intermediates to be modulated and suppressing hydrogen production. Thus, this study provides a strategy in the design of electrocatalysts in electrochemical nitrate reduction.

codoping | ammonium | electrocatalysis | selectivity | MOF

Due to the rising threat of global pollution and rapid depletion of fossil fuels, there is an urgent requirement to exploit clean, safe, and sustainable energy sources (1, 2). Ammonia (NH_3) is crucial for the production of agricultural fertilizers and can be used as a green hydrogen-rich fuel (3). In addition, it is a key raw material for fine chemicals and fuels (4). NH_3 is synthesized using the Haber–Bosch process (5, 6) from dinitrogen and hydrogen at high temperatures and pressures (7, 8). However, this process is energy intensive, requiring ~2% of the total global power generation (9). In addition, the production of hydrogen from fossil fuels produces greenhouse gases (10, 11). Therefore, the use of nitrogen with water as a hydrogen source to produce NH_3 via electrocatalytic (photocatalytic) nitrogen reduction has attracted considerable attention (12, 13). Despite years of development, this process still has low activity, faradaic efficiency (FE), and selectivity for NH_3 production because of the strong N≡N bonds (941 kJ mol^{-1}) (14), competitive hydrogen evolution reaction (HER), sluggish kinetics (15), and low energy efficiency (16–18). Thus, new routes for ammonia synthesis under mild conditions are required.

Nitrate is ubiquitous in water bodies. However, human activities have polluted surface and groundwater with excess nitrate (19, 20), resulting in eutrophication. The accumulation of nitrate can cause serious diseases, thus posing a threat to human health (21, 22), which is why nitrate-removal methods have attracted increasing attention (23). Therefore, from an environmental and energetic point of view, the conversion of waste aqueous nitrate into value-added products, such as recycled ammonia solution, is attractive. The electrochemical nitrate reduction reaction (NO_3^-RR) is a promising route to produce NH_3 because of the moderate operating conditions and decent efficiency (24). Recently, the activities and selectivities of transition metals for NO_3^-RR to recycled ammonia have been extensively studied (9, 25, 26), revealing that the use of NO_3^- for large-scale green NH_3 production could save energy and reduce pollution.

However, the low activity and selectivity, as well as instability, of electrocatalysts have hindered the use of NO_3^-RR. Specifically, the conversion of NO_3^- to NH_3 involves an eight-electron transfer reaction, and crucially, the HER is competitive. Furthermore, the potential for the NO_3^- to NH_3 reaction is usually lower than that of the HER, resulting in H_2 generation, consumption of electron donors, and thus, relatively low selectivity and FE (27). Therefore, catalysts that disfavor N≡N bond formation and the HER are required to improve NO_3^- to NH_3 efficiently and selectively.

Recently, carbon-coated iron nanomaterials have been found to show competitive performance to noble metal catalysts in NO_3^-RR applications (21, 28, 29). Nevertheless, the NO_3^- removal efficiency and NH_3 selectivity of these reported Fe-based electrocatalysts are still far from satisfactory. The main drivers of this phenomenon are listed here. First, the high corrosion and dissolution of Fe-based catalysts are significant drawbacks, which seriously reduce the stability of the electrode, especially over prolonged use. Moreover, the conventional

Significance

Electrochemical reduction of nitrate pollution in water into value-added ammonium is essential for modern agriculture and industry and represents a potentially sustainable strategy to replace the traditional Haber–Bosch process. However, the nitrate reduction reaction (NO_3^-RR) process under ambient conditions often suffers from low selectivity. Here, we developed a strategy of tuning an electronic structure for preparing cobalt-doped Fe@Fe_2O_3 electrocatalysts. Cobalt doping tunes the Fe d-band center, thereby modulating the adsorption energies of intermediates and suppressing hydrogen production. Therefore, the electrocatalysts exhibit superior NO_3^-RR activity with a high nitrate removal capacity (100.8 mg N g_{cat}^{-1} h^{-1}), NH_3 selectivity (99.0 ± 0.1%), and faradaic efficiency (85.2 ± 0.6%). This strategy provides an approach to design advanced materials for NO_3^-RR.

Author contributions: S.Z. and M.L. designed research; S.Z. and M.L. performed research; S.Z., M.L., and J.L. contributed new reagents/analytic tools; S.Z., M.L., J.L., Q.S., and X.L. analyzed data; and S.Z. and M.L. wrote the paper.

The authors declare no competing interest.

This article is a PNAS Direct Submission.

[1]To whom correspondence may be addressed. Email: miaoli@tsinghua.edu.cn.

This article contains supporting information online at http://www.pnas.org/lookup/suppl/doi:10.1073/pnas.2115504119/-/DCSupplemental.

Published January 31, 2022.

carbon coating synthesis method lacks precise control and leads to uneven carbon encapsulation, reducing catalyst reactivity and stability (20, 30). Second, nanostructured Fe-based catalysts can easily aggregate due to their natural magnetic properties and high surface energy, which hinders surface active sites (21). Third, the d-electrons of transition metals are prone to the formation of metal–H bonds for competitive HER, leading to a low selectivity and low catalytic efficiency (31). Thus, a rational design to tailor material properties has drawn attention. Because of their diverse and tunable structures and compositions, metal–organic frameworks (MOFs) have attracted significant attention in chemistry and materials science (32–34). MOF precursors can be used to form metal-based catalysts and carbon materials having good electrocatalytic activity via pyrolysis or chemical reactions (35, 36). Importantly, MOF-derived porous graphitic carbon-coated nanoparticles (NPs) have a lower tendency to agglomerate and higher reactivity than traditional materials as well as high structural and compositional integrity during catalytic reduction (37). Moreover, heteroatom doping can be exploited to tune the intrinsic conductivity and electronic structure, thus enhancing catalytic performance (38). For most heterogeneous catalysts, the electronic structure uniquely determines the inherent adsorption ability for intermediates (38). Thus, by tuning the electronic band structure, the catalytic performance can be controlled. In addition, dopants change the electronic environment around the doping site, generating new catalytic active sites and increasing catalytic activity (39–42). Additionally, cobalt has emerged as a promising candidate for dopant that can adjust the electronic structure owing to its higher FE (7) and higher NH_3 selectivity at a negative potential (24).

Herein, we report on Fe@Fe_2O_3 NPs doped with Co encapsulated in porous graphitic carbon derived from Fe-MOF (denoted Co-Fe@Fe_2O_3) for the NO_3^-RR. Co-Fe@Fe_2O_3 shows a high nitrate removal capacity (100.8 mg N g_{cat}^{-1} h^{-1}), high ammonia selectivity (99.0 ± 0.1%), and a very high FE (85.2 ± 0.6%). The Co-Fe@Fe_2O_3 NPs were obtained by pyrolyzing transition metal–doped Fe-MOF-74. The Co dopes Fe sites in the Fe_2O_3 lattice, forming a single phase with little structural change. Furthermore, ^{15}N isotope–labeling experiments revealed that the produced ammonia originated from nitrate reduction. Density functional theory (DFT) calculations also revealed the effect of Co doping on catalytic performance, revealing that it causes a shift of the d-band center of Fe, which changes the adsorption energy of intermediates and products, thus enhancing catalytic performance for the NO_3^-RR.

Results and Discussion

Catalyst Synthesis. MOF-74 was selected as the precursor because of its porous architecture, large surface area, and easy preparation of mixed metal MOFs (43). Fe-MOF was prepared with a small quantity of Co-MOF (Fig. 1*A*) to yield cobalt-doped Fe-MOF. First, we synthesized Co-MOF based on Co^{2+} and 2,5-dihydroxyterephthalic acid (H_4DOBDC) employing the solvothermal method. Second, small amounts of Co-MOF and Fe^{2+} were used as precursors of the Co and Fe atoms to synthesize a cobalt-doped iron-based MOF so as to replace Fe with a small amount of cobalt. Finally, pyrolysis in argon converted the organic ligands in the MOF to porous graphitic carbon and metal ions to uniformly dispersed Co-doped Fe@Fe_2O_3 NPs embedded in the carbon (denoted Co-Fe@Fe_2O_3). The high density of catalytically active sites and the porous conductive matrix of the Co-Fe@Fe_2O_3 NPs resulted in excellent electrocatalytic performance, with enhanced NH_3 selectivity and FE. For comparison, a carbon-embedded pure Co NP catalyst prepared from Co-MOF-74 (referred to as Co NPs subsequently), a nondoped Fe@Fe_2O_3 catalyst, and Co-Fe@Fe_2O_3-t (where t is the pyrolysis temperature) catalysts were synthesized (*Materials and Methods*).

Catalyst Characterization. The morphologies of Co-Fe@Fe_2O_3 and the precursor MOF were observed using field emission scanning electron microscopy (FESEM) and high-resolution transmission electron microscopy (HRTEM) (Fig. 1). The Co-doped Fe-MOF-74 has a porous spherical-like morphology (*SI Appendix*, Fig. S1). After pyrolysis at 900 °C, the resultant Co-Fe@Fe_2O_3 comprised flower-like nanospheres 1 μm in diameter (Fig. 1B), having a similar morphology to that of the Co-doped Fe-MOF despite some cracks on the surface. The heterostructure of Co-Fe@Fe_2O_3 was investigated further using transmission electron microscopy (TEM) (Fig. 1*C*) and HRTEM (Fig. 1 *D* and *F*). Before analysis, the samples were ground in a mortar. The TEM image shows a large number of Co-Fe@Fe_2O_3 NPs encapsulated in the graphitic carbon layers. The HRTEM images show that the carbon shell lattice is consistent with the (002) plane of graphitic carbon, and the carbon layer coated on the Co-Fe@Fe_2O_3 NPs is more graphitic than that far from the Co-Fe@Fe_2O_3 NPs, probably because the NPs catalyze carbon graphitization. In the HRTEM and fast Fourier transform (FFT) images of the Co-Fe@Fe_2O_3 NPs, lattice fringes of the Co-Fe@Fe_2O_3 NPs (Fig. 1 *D*–*F*) can be seen, having spacings of 0.207 and 0.184 nm, corresponding to the (024) and (202) planes, respectively, of Fe_2O_3 (Fig. 1 *D* and *E*). The lattice fringe spacing of 0.202 nm can be ascribed to the (110) face of metallic a-Fe (Fig. 1*F*). As shown in the images, the Fe NPs were covered by Fe_2O_3 shells. This metallic Fe core with a semiconducting Fe_2O_3 shell is expected to enhance the catalytic activity via formation of a Schottky barrier between Fe and Fe_2O_3, which is favorable for charge separation. The scanning TEM and X-ray spectroscopy (EDX) elemental mapping images confirm the presence of C, O, Fe, and Co (Fig. 1*G* and *SI Appendix*, Fig. S3). Additionally, a line profile extracted from the EDX confirms the unique heterostructure discussed above (*SI Appendix*, Fig. S2). Moreover, inductively coupled plasma measurements quantified the metal contents in Co-Fe@Fe_2O_3, revealing Fe and Co contents of 70.9 and 1.85 wt %, respectively. Nitrogen adsorption/desorption isotherms (*SI Appendix*, Fig. S4) confirmed that the prepared Co-doped Fe-MOF, Co-Fe@Fe_2O_3, Fe@Fe_2O_3, and Co NPs are porous, having Brunauer–Emmett–Teller (BET) surface areas of 350.12, 19.79, 172.8, and 137.89 m^2 g^{-1}, respectively, and that Co-Fe@Fe_2O_3 has a mesoporous structure arising from the nanoflower morphology induced by high-temperature pyrolysis. This morphology results in abundant interlayer mesopores in the particle interior, which is promising from the perspective of exposing active sites and promoting electrolyte transport and thus, electrocatalytic activity.

The X-ray diffraction (XRD) patterns of Co-Fe@Fe_2O_3 (Fig. 2*A*) and Fe@Fe_2O_3 (*SI Appendix*, Fig. S5) reveal the presence of Fe and Fe_2O_3, and the peaks at 44°, 65°, and 82° correspond to the (110), (200), and (220) planes, respectively, of alpha-Fe (Powder Diffraction File #06–0696). The other peaks are typical of crystalline Fe_2O_3 (Powder Diffraction File #33–0664), confirming the presence of Fe_2O_3. The XRD pattern of the pure Co NPs contains (111), (200), and (220) reflections consistent with metallic Co (*SI Appendix*, Fig. S5). The chemical environments and electronic structure of the Co, Fe, C, and O in Co-Fe@Fe_2O_3 were analyzed using X-ray photoelectron spectroscopy (XPS) between 0 and 1,200 eV. The XPS survey spectrum contains sharp peaks at 284.5, 532.8, and 780.1 eV corresponding to C 1s, O 1s, and Fe 2p, respectively. The weight ratio of the Co dopant in Fe@Fe_2O_3 was only 1.85%, so the Co 2p peak was not observed in the survey spectrum. However, the Co 2p spectrum for Co-Fe@Fe_2O_3 (Fig. 2*B*) contains peaks at 796.4 eV consistent with Co ($2p_{1/2}$) and at 786.8 and 802.2 eV, corresponding to

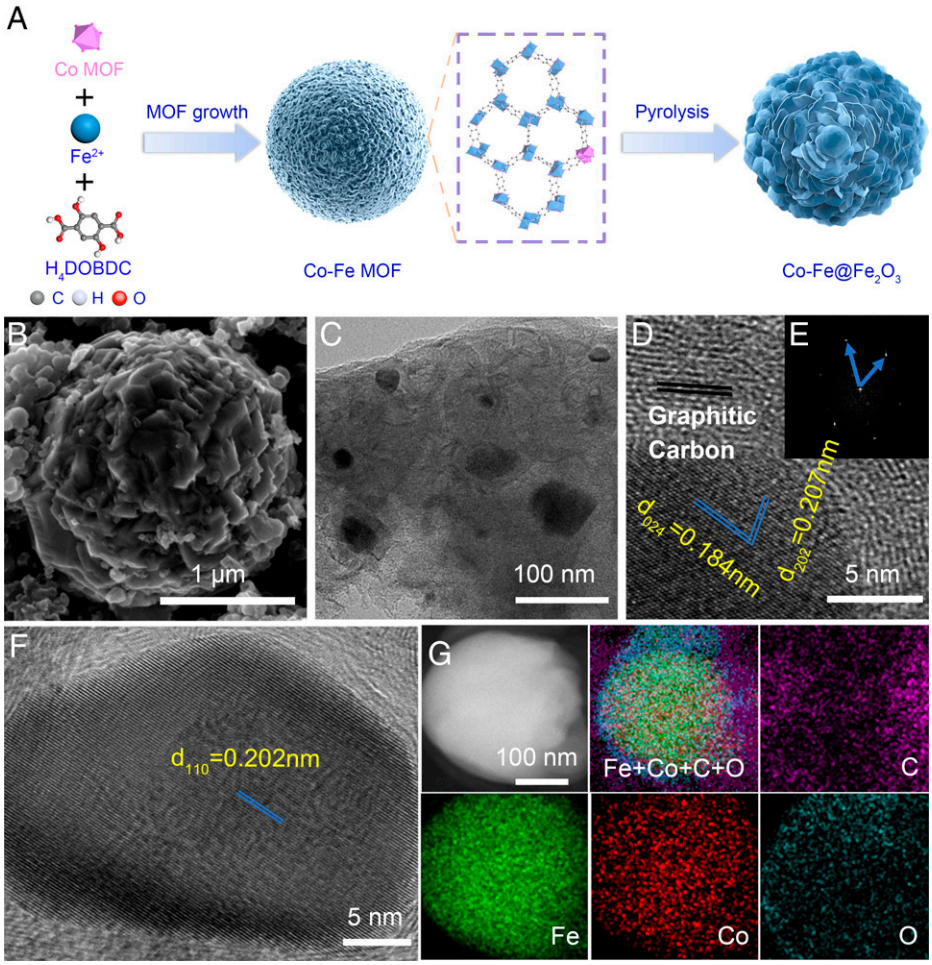

Fig. 1. Synthesis and morphology of Co-Fe@Fe_2O_3. (*A*) Synthetic procedure. (*B*) FESEM image. (*C*) TEM image. (*D* and *F*) HRTEM image. (*E*) FFT image. (*G*) EDX elemental maps of C, O, Co, and Fe.

the shake-up satellite peaks of Co^{2+}. In addition, a peak corresponding to Co^{2+} was observed at 781.5 eV. Therefore, the Co dopant in Fe@Fe_2O_3 NPs is in the ionic state. The Fe 2p spectrum of Co-Fe@Fe_2O_3 (Fig. 2*C*) shows peaks at 711 eV (Fe $2p_{3/2}$) and 724 eV (Fe $2p_{1/2}$) (28). Satellite peaks are at 719.4 and 733.0 eV. Peaks at 710.5 eV (Fe^{2+}) and 712.3 eV (Fe^{2+}) correspond to the Fe $2p_{3/2}$ orbitals, while the other peaks at 723.9 eV (Fe^{2+}) and 725.8 eV (Fe^{2+}) can be attributed to the Fe $2p_{1/2}$ orbitals. However, no obvious Fe^0 peak was observed, indicating that the iron in the surface region is present as iron oxide, consistent with the XRD data. The O 1s spectrum (*SI Appendix*, Fig. S6*C*) indicates the presence of the metal–O bond (530.0 eV) in the Fe_2O_3 or CoO (44). The C-OH and C-COOH (532.0 and 533.2 eV, respectively) peaks are originated from the pyrolysis of Co-doped Fe-MOF-74. For the C 1s spectrum in *SI Appendix*, Fig. S6*B*, peaks at 284.7 and 288.9 eV are attributed to the C = C and O-C = O bonds, and the C-C peaks are at 285.6 and 284.3 eV, respectively (45).

X-ray absorption fine structure (EXAFS) spectra were obtained to reveal the structure and coordination environment of Co and Fe atoms in Co-Fe@Fe_2O_3 (Fig. 2 *D*–*I*). As shown in the X-ray absorption near-edge structure (XANES), the analysis of Co-Fe@Fe_2O_3 and reference samples reveals that Fe has two valence states, Fe^0 and Fe^{3+}. The white line peak intensity for Co-Fe@Fe_2O_3 is markedly higher than that of Fe foil, confirming that there is an oxidation state on the Fe surface (46), consistent with the XPS results. The peaks at ~2.20 and 1.49 Å in the Fourier-transformed k^3-weighted extended EXAFS spectrum (Fig. 2*E*) can be assigned to Fe-Fe and Fe-O bonds, respectively (47). The former implies elemental iron, whereas the latter implies Fe_2O_3. Consistent with the TEM, XPS, and XRD data, this result suggests that the metallic iron core is covered with an Fe_2O_3 layer. The XANES spectra at the Co K edge reveal that the energy absorption threshold for Co-Fe@Fe_2O_3 is higher than that of Co foil, and the energy absorption threshold of Co-Fe@Fe_2O_3 is much closer to that of CoO, again suggesting the ionic state of cobalt in Co-Fe@Fe_2O_3 (48). Additional structural information about the Co atoms was obtained by EXAFS. Fig. 2*H* shows the Fourier-transformed k^3-weighted $\chi(k)$ function of the EXAFS spectra for Co-Fe@Fe_2O_3, CoO, and Co foil. The dominant peak in the functions for Co-Fe@Fe_2O_3 and CoO is at 1.5 Å, consistent with Co-O bonds (49). In addition, there is no Co-Co peak at 2.16 Å, which would indicate metallic Co, suggesting that the Co in Co-Fe@Fe_2O_3 is present in the oxide layer on the catalyst surface. *SI Appendix*, Table S1 summarizes the results of fitting the EXAFS spectrum of Co-Fe@Fe_2O_3 for bond analysis. These data (Fig. 2 *F* and *I* and *SI Appendix*, Fig. S7) also indicate that Co was incorporated into Fe_2O_3 as CoO, as also shown by the XPS results.

NO_3^-RR Activity and Electrochemical Analysis. The prepared electrocatalysts were used to modify nickel foam electrodes and tested for NO_3^-RR activity in a neutral electrolyte [50 ppm NO_3^-N ($NaNO_3$) and 0.1 M Na_2SO_4] for 10 h using a three-electrode system (*Materials and Methods* and *SI Appendix*, Fig. S8). In addition, electrocatalytic tests combining chronoamperometry and

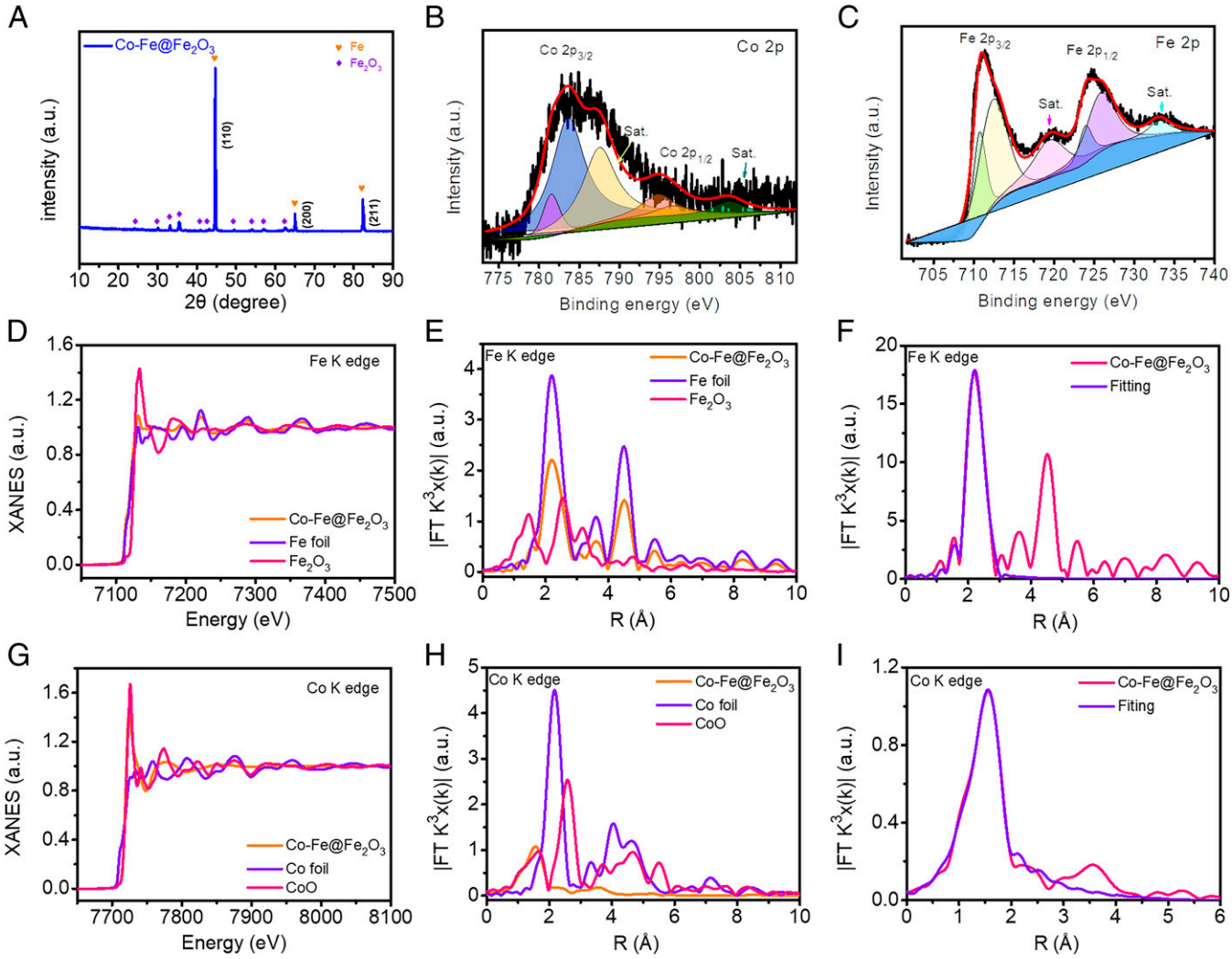

Fig. 2. Characterization of Co-Fe@Fe_2O_3. (*A*) XRD pattern. (*B*) Fe 2p and (*C*) Co 2p XPS spectra. (*D*) Fe K-edge XANES spectra, (*E*) Fourier-transformed (FT) Fe K-edge EXAFS spectra, and (*F*) corresponding FT-EXAFS fitted curves. (*G*) Co K-edge XANES spectra, (*H*) FT Co K-edge EXAFS spectra, and (*I*) corresponding FT-EXAFS fitted curves.

ultraviolet-visible (UV-vis) spectroscopy were carried out using the same electrolyte at −0.645 V (vs. the reversible hydrogen electrode [RHE]). After electrocatalytic NO_3^-RR for 10 h, the as-used electrolyte was collected to quantify the NO_3^-, NH_4^+, and NO_2^- concentrations using the colorimetry method (*Materials and Methods*), and the calibration curves are shown in *SI Appendix*, Fig. S9. As shown in *SI Appendix*, Fig. S10, the nitrate removal efficiency and NH_3 selectivity increased with prolonged electrolysis time. The Co-Fe@Fe_2O_3 showed the best performance: 96.7 ± 0.2% nitrate removal and 99.0 ± 0.1% NH_3 selectivity after 10 h, suggesting that Co-Fe@Fe_2O_3 exhibits excellent electrocatalytic properties. These performance metrics are much better than those of reported iron-based and other metal catalysts (*SI Appendix*, Table S2). In contrast, the values for the Fe@Fe_2O_3 catalyst (without the Co dopant), which had a larger surface area and pore volume, were 86.1 ± 4.0% and 92.7 ± 1.2%, respectively (Fig. 3*A*).

Heteroatom doping modifies the electronic structure and affects catalytic performances, but the pyrolysis temperature can also have an effect. Notably, the NO_3^- removal efficiency and NH_3 selectivity of the Co-Fe@Fe_2O_3-t catalyst after 10 h improved with an increase in pyrolysis temperature, and the sample pyrolyzed at 900 °C yielded the highest values (Fig. 3*B*), suggesting that graphitic carbon is crucial for NO_3^-RR activity, consistent with previous reports (50). However, the NO_3^-RR performance of Co-Fe@Fe_2O_3-1,000 was lower, possibly due to the decreased surface area and structural collapse (51). Notably, a small amount of the Co-Fe@Fe_2O_3-900 catalyst achieved 1,008.0 ± 3.4 mg N g_{cat}^{-1} denitrification in 10 h (Fig. 3 *D* and *E*), much higher than those of Fe@Fe_2O_3 (897.0 ± 42.1 mg N g_{cat}^{-1}), pure Co NPs (873.6 ± 43.2 mg N g_{cat}^{-1}), and other Co-Fe@Fe_2O_3-t (Co-Fe@Fe_2O_3-600: 942.5 ± 22.0 mg N g_{cat}^{-1}; Co-Fe@Fe_2O_3-700: 987.4 ± 11.1 mg N g_{cat}^{-1}; Co-Fe@Fe_2O_3-800: 993.1 ± 27.8 mg N g_{cat}^{-1}; Co-Fe@Fe_2O_3-1,000: 972.2 ± 6.9 mg N g_{cat}^{-1}) catalysts. Fig. 3*C* and *SI Appendix*, Fig. S11 show the change in NO_3^-, NO_2^-, and NH_4^+ concentrations with time. At a constant voltage of −0.645 V (vs. RHE), the NO_3^--N concentration decreased from 50.35 to 1.61 ppm over 10 h using the Co-Fe@Fe_2O_3-900 catalyst, and the NO_3^- conversion was ∼96.7 ± 0.2%. The NH_4^+ concentration increased steadily and reached 48.65 ppm after 10 h, indicating nitrate-to-ammonium conversion. Meanwhile, the intermediate NO_2^- concentration was negligible during the reaction, indicating high ammonium selectivity. The catalytic performances of Co, Fe@Fe_2O_3, and Co-Fe@Fe_2O_3-t were studied for comparison (*SI Appendix*, Figs. S12 and S13). The NO_3^- conversion rate and NH_3 production rate of Co-Fe@Fe_2O_3-900 are significantly

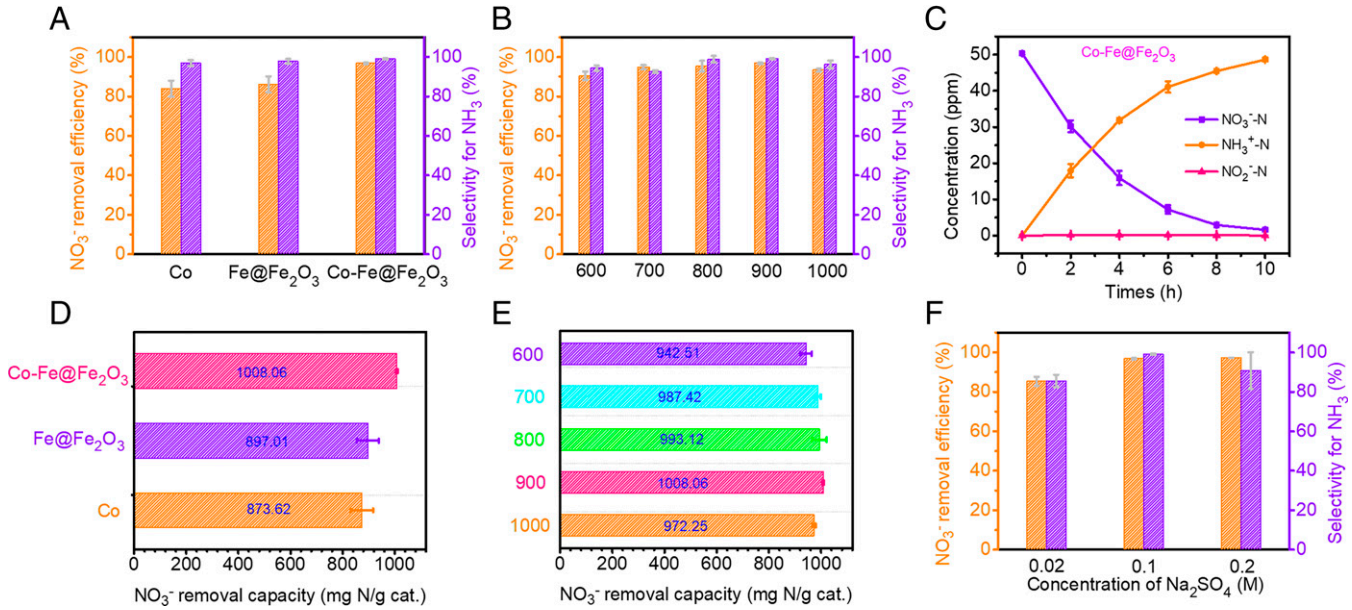

Fig. 3. Nitrate removal performance. (*A* and *B*) Nitrate removal efficiencies and NH_3 selectivities of catalysts. (*C*) Time-dependent concentrations of NO_3^-, NO_2^-, and NH_3 over Co-Fe@Fe_2O_3. (*D* and *E*) Nitrate removal capacities of catalysts. (*F*) Nitrate removal efficiencies and NH_3 selectivities with different concentrations of Na_2SO_4. Reaction conditions: initial NO_3^--N concentration, 50 ppm; −0.645 V vs. RHE, 0.1 M Na_2SO_4, 10 h.

higher than those of Co, Fe@Fe_2O_3, and Co-Fe@Fe_2O_3-t, and Co-Fe@Fe_2O_3-900 showed the lowest nitrite yield after NO_3^-RR.

Moreover, very high (0.2 M) or low (0.02 M) concentrations of Na_2SO_4 were not favorable for the NO_3^-RR (Fig. 3*F*) because the former causes competitive anion adsorption on active sites, whereas the latter reduces electrolyte conductivity.

Cyclic voltammetry (CV) measurements were used to evaluate the NO_3^-RR activities of Co-Fe@Fe_2O_3, Fe@Fe_2O_3, and Co (*SI Appendix*, Fig. S14). At a scan rate of 50 mV s^{-1}, an apparent oxygen reduction peak was observed in aqueous 0.1 M Na_2SO_4 with 500 ppm NO_3^--N but disappeared in aqueous 0.1 M Na_2SO_4 without NO_3^--N, indicating the reduction of nitrate to nitrite. The oxygen reduction peak occurred at −0.55 V vs. RHE for the Co-Fe@Fe_2O_3 catalyst, demonstrating that the Co dopant and mesoporous carbon enhance the NO_3^-RR performance. In addition, the electrochemical catalytic activities of Co-Fe@Fe_2O_3, Fe@Fe_2O_3, and Co were measured by linear sweep voltammetry (LSV) at a scan rate of 10 mV s^{-1} in 0.1 M Na_2SO_4 electrolyte with and without NO_3^--N, revealing clear peaks at −0.3 and −0.5 V (vs. RHE) resulting from the electroreduction of adsorbed nitrate ions. As shown in Fig. 4*A*, Co-Fe@Fe_2O_3 has an onset potential of −0.65 V (vs. RHE) and a limiting current density of 23.28 mA cm^{-2} in 0.1 M Na_2SO_4 in the presence of nitrate, comparable with that obtained in 0.1 M Na_2SO_4 electrolyte without nitrate, demonstrating the remarkable catalytic activity for the NO_3^-RR. In addition, the current density of the Co-Fe@Fe_2O_3 catalyst was higher at high NO_3^--N concentrations than at low concentrations (*SI Appendix*, Fig. S16*A*). Furthermore, NO_3^-RR electrolysis tests were performed at the various potential and electrolyte concentrations to investigate the catalytic activity and the optimum working potential of the Co-Fe@Fe_2O_3 catalyst for electrochemical NH_3 synthesis. *SI Appendix*, Fig. S15 shows the corresponding chronoamperometry curves within the potential range of 0.55 to 0.95 V vs. RHE, and electrolyte concentrations range from 50 to 1,000 ppm. The current density remained steady, indicating the good chemical stability of the Co-Fe@Fe_2O_3 catalyst during the electrochemical NO_3^-RR tests. The slight fluctuations of the current density at −0.75 and −0.95 V vs. RHE can be attributed to the bubbles on the electrode surface produced by the dominant HER at the lower potential. After electrocatalytic NO_3^-RR for 4 h, the electrolyte was collected to quantify the produced NH_3 by the colorimetry method. From −0.445 to −0.945 V, the NH_3 yield rate gradually increased, whereas the FE displayed a volcano shape, having its maximum of 85.2 ± 0.6% at −0.75 V (Fig. 4*B*). At different NO_3^- concentrations, the potential conditions required to maximize the FE differed. Specifically, at 50, 200, 500, and 1,000 ppm NO_3^-, the FE was maximized at −0.55, −0.75, −0.75, and −0.55 V, respectively. Combining the NH_3 selectivity and FE results, the optimum NO_3^-RR activity of Co-Fe@Fe_2O_3 was achieved at −0.75 V vs. RHE in 0.1 M Na_2SO_4 electrolyte containing 500 ppm NO_3^--N, yielding an NH_3 selectivity of 94.6 ± 1.1% and FE of 85.2 ± 0.6% (Fig. 4*C*). When the NO_3^--N concentration was increased to 1,000 ppm, NH_3 selectivity dropped only slightly, demonstrating the wide range of applicable concentrations. As the cathodic potential was increased, the NH_3 yield rate gradually increased, reaching a maximum of 1,505.9 ± 130.5 μg h^{-1} cm^{-2} at −0.95 V vs. RHE. However, the FE and NH_3 selectivity gradually declined at -0.95 V vs. RHE because of increasing competition with the HER at high potentials.

The NO_3^-RR performances of Co, Fe@Fe_2O_3, and Co-Fe@Fe_2O_3 are shown in Fig. 4*E*, revealing the effect of cobalt doping. All electrodes reduced NO_3^- to NH_3, and the NH_3 selectivity, FE, and NH_3 yield rate of Co-Fe@Fe_2O_3 were 94.6 ± 1.1%, 85.2 ± 0.6%, and 880.5 ± 38.0 μg h^{-1} cm^{-2}, respectively, much higher than those of the Co NPs (94.3± 0.9%, 77.1± 0.4%, and 866.1± 88.7 μg h^{-1} cm^{-2}, respectively) and Fe@Fe_2O_3 (81.8 ± 2.9%, 79.1 ± 3.2%, and 561.1 ± 117.8 μg h^{-1} cm^{-2}, respectively). Notably, the NH_3 selectivity of Co-Fe@Fe_2O_3 is much better than those of reported NO_3^-RR catalysts (*SI Appendix*, Table S3). Additionally, we compared the energy efficiency (EE) of Co, Fe@Fe_2O_3, and Co-Fe@Fe_2O_3. Consequently, we achieved an NH_3 half-cell EE of 23% using Co-Fe@Fe_2O_3 in 500 ppm of NO_3^- (*SI Appendix*, Fig. S17), which is higher than that of the Co and Fe@Fe_2O_3 catalysts.

The Tafel slope of 70.73 mV dec^{-1} for Co-Fe@Fe_2O_3 is smaller than those for Fe@Fe_2O_3 (87.78 mV dec^{-1}) and Co

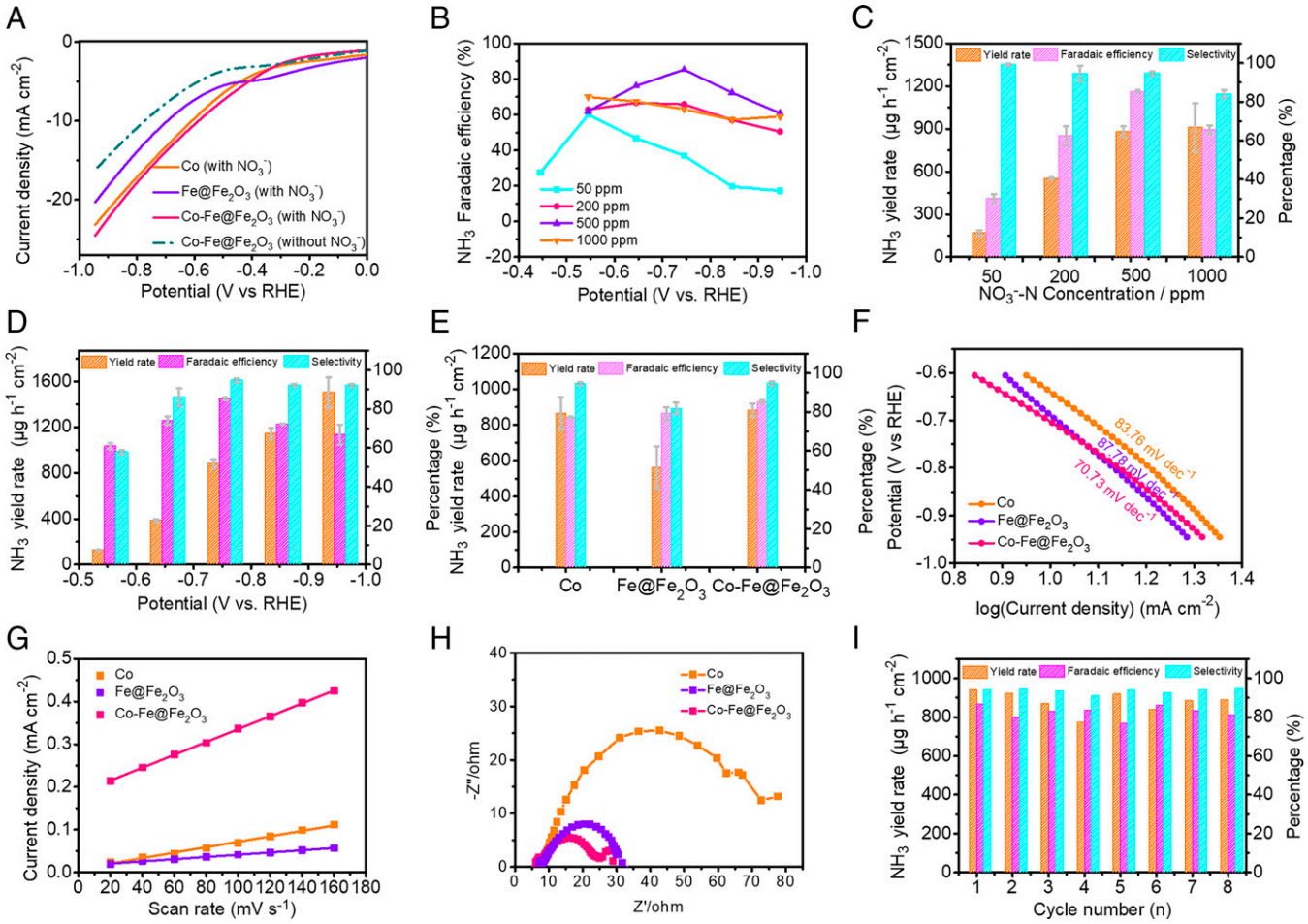

Fig. 4. Electrochemical performances of catalysts for 4 h of NO_3^-RR electrolysis. (*A*) LSV curves of Co-Fe@Fe_2O_3, Fe@Fe_2O_3, and Co in 0.1 M Na_2SO_4 solution with and without NO_3^--N (500 ppm). (*B*) FE of NH_3 on the Co-Fe@Fe_2O_3 catalyst with different NO_3 concentrations. (*C*) Comparison of the highest FE, yield rate, and NH_3 selectivity for the Co-Fe@Fe_2O_3 catalyst at different NO_3 concentrations. (*D*) Potential-dependent FE, NH_3 yield rate, and NH_3 selectivity for Co-Fe@Fe_2O_3. Comparison of (*E*) FE, NH_3 yield rate, and NH_3 selectivity; (*F*) Tafel plots; (*G*) C_{dl} values; and (*H*) Nyquist plots for Co-Fe@Fe_2O_3, Fe@Fe_2O_3, and Co NPs. (*I*) Consecutive recycling test at −0.745 V for Co-Fe@Fe_2O_3.

(83.76 mV dec^{-1}), further indicating the faster NO_3^-RR kinetics of Co-Fe@Fe_2O_3 (Fig. 4*F*).

The electrochemical surface areas (ECSAs), which are related to catalytic activity, of the catalysts were calculated using CV measurements from 0.435 to 0.535 V vs. RHE at different scan rates (*SI Appendix*, Fig. S18). No significant faraday currents were observed. As shown in Fig. 4*G*, the Co-Fe@Fe_2O_3 NPs (37.75 cm^2_{ECSA}) has a higher ECSA than Fe@Fe_2O_3 (6.5 cm^2_{ECSA}) and Co (15.9 cm^2_{ECSA}), suggesting that Co doping increases the ECSA and thus, has a positive impact on the NO_3^-RR activity. Next, electrochemical impedance spectroscopy was used to obtain Nyquist plots for Co-Fe@Fe_2O_3, Fe@Fe_2O_3, and Co NPs (Fig. 4*H*). The semicircle radius is related to the charge transfer resistance, and a smaller arc radius indicates faster interfacial electron transfer. The Nyquist plots indicate that Co doping affected the electrochemical properties of the electrodes significantly; the arc radius of Co-Fe@Fe_2O_3 was the smallest of those of the produced catalysts, indicating low charge-transfer resistance and suggesting that Co doping can promote charge transfer in the cathode, which is conducive for NO_3^- reduction. After eight cyclic chronoamperometric runs using Co-Fe@Fe_2O_3 (Fig. 4*I*), the NH_3 selectivity, FE, and NH_3 yield rate showed no obvious decay, confirming its excellent electrocatalytic stability. These results suggest that the excellent NO_3^-RR activity of Co-Fe@Fe_2O_3 is associated with its unique structure and porous carbon encapsulation, suggesting that this is a favorable approach to achieve effective and highly selective NO_3^-RR. In particular, carbon encapsulation enhances the conductivity of Co-Fe@Fe_2O_3, maintains its structural integrity, shortens the ion-diffusion pathways, and enhances stability.

To further prove the stability of Co-Fe@Fe_2O_3 during NO_3^-RR, the structure and valence states of Co-Fe@Fe_2O_3 before and after NO_3^-RR were probed by TEM, HRTEM, XPS, and XRD. The catalyst coated on the nickel foam was collected by ultrasonication in ethanol to measure TEM and HRTEM, while the catalyst coated on the nickel foam was directly used to measure XRD and XPS. As shown in *SI Appendix*, Fig. S19*A*, TEM images showed that the structure of the carbon-coated Co-Fe@Fe_2O_3 NPs was well maintained after the NO_3^-RR tests. Meanwhile, the lattice fringes in the HRTEM image (*SI Appendix*, Fig. S19 *B* and *C*) of Co-Fe@Fe_2O_3 also confirm the crystal structures of Fe_2O_3 and graphitic carbon with lattice spacing of 0.251 and 0.35 nm, which are indexed to the corresponding (110) plane of the Fe_2O_3 crystal phase and to the (002) plane of graphitic carbon, respectively. This proves that the structure of the Co-Fe@Fe_2O_3 is maintained after the NO_3^-RR process. Moreover, the recycled Co-Fe@Fe_2O_3 catalyst showed no substantial difference compared with unreacted catalyst during the electrocatalytic NO_3^-RR

process, which was confirmed by comparing the Fe 2p XPS spectra (*SI Appendix*, Fig. S20). This demonstrates the good stability of our catalyst. In addition, we performed additional XRD characterization of Co-Fe@Fe_2O_3 before and after NO_3^-RR to provide convincing evidence that the heterostructure remains after the NO_3^-RR reaction. As shown in *SI Appendix*, Fig. S21*A*, the characteristic diffraction peaks of α-Fe were identified in the XRD pattern. We added the XRD patterns that partially amplify the peaks at 20° to 40° (*SI Appendix*, Fig. S21*B*) and 60° to 90° (*SI Appendix*, Fig. S21*C*) of *SI Appendix*, Fig. S21*A*. The characteristic diffraction peaks of iron oxide and α-Fe were identified. Other than the three peaks assigned to the nickel foam substrate, the peak positions before and after the NO_3^-RR reaction agree well with each other. This indicates that the crystal phase of Co-Fe@Fe_2O_3 does not change after the electrocatalytic reaction, which further proves the stability of the catalyst. Therefore, MOF-derived Co-Fe@Fe_2O_3 was used as an efficient catalyst for NO_3^-RR with good structural stability and excellent durability.

Origin of Nitrogen in Ammonia. To exclude other potential nitrogen sources, such as the catalyst, electrolyte, or laboratory environment that could affect the NO_3^-RR results, tests in nitrate-free Na_2SO_4 solution were conducted to verify that the source of ammonia was the $^{14}NO_3$ starting material in the electrolyte. Negligible ammonia generation was observed (*SI Appendix*, Fig. S16*B*). In addition, a ^{15}N isotopic labeling with ^{1}H-NMR observation was used to confirm the origin of the produced NH_3. As shown in Fig. 5*A*, after electrochemical NO_3^-RR using $Na^{15}NO_3$ as the electrolyte, a doublet corresponding to $^{15}NH_4^+$ at δ = 6.98 and 7.10 ppm appeared; in contrast, when $Na^{14}NO_3$ was used, a triplet corresponding to $^{14}NH_4^+$ at δ = 6.99, 7.06, and 7.13 ppm was observed (Fig. 5*B*). Thus, the produced NH_3 was derived from the NO_3^-RR. To quantify the NH_3 derived from NO_3^-RR, maleic acid ($C_4H_4O_4$) was used as an external standard. Using a standard curve based on peak integral ratios (NH_4^+-N/$C_4H_4O_4$) and the NH_4^+-N concentration, the generated ammonium in the electrolyte was quantified (Fig. 5 *D* and *E*). The NMR-derived production rates of $^{15}NH_3$ and $^{14}NH_3$ after 4 h were consistent with the UV-vis results (Fig. 5 *C*–*F*), confirming the reliability of these ammonium quantitation methods. In addition, the FE was calculated to be 79.3% by ^{1}H-NMR (confer 80.1% by UV-vis).

Mechanistic Study. A catalyst combining high NO_3^- adsorption with a poor rate of direct H^+ to H_2 conversion should show high reaction selectivity and FE. Thus, DFT calculations were conducted to understand how Co doping promotes the NO_3^-RR activity of Co-Fe@Fe_2O_3. Specifically, we analyzed the preferential adsorption of NO_3^- on Co-Fe@Fe_2O_3, as well as its inhibitory effect on the HER, using a model based on the (001) plane of Fe_2O_3 with 1.85 wt % Co and an Fe (111) base layer. Structural optimization of Co-Fe@Fe_2O_3 (Fig. 6*A*), as well as Fe@Fe_2O_3 (Fig. 6*B*), and Co (Fig. 6*C*) models was carried out, and the H^+ and NO_3^- adsorption energies and the H_2 formation energies were calculated. In NO_3^-RR, the first and arguably the most important step is NO_3^- adsorption. The favorable adsorption of NO_3^- is crucial, affecting the subsequent reduction of NO_3^- in the presence of H^+ and inhibiting the competitive adsorption of other anions. However, strong adsorption hinders intermediate desorption, whereas weak adsorption limits electron and proton transfer to the adsorbed intermediates. As shown in *SI Appendix*, Fig. S22, the adsorption energy (E_{ads}) of $*NO_3^-$ (where the asterisk indicates an adsorbed species) on Co-Fe@Fe_2O_3 of −2.60 eV is more positive than that of Co (−2.43 eV) and more negative than that of Fe@Fe_2O_3 (−2.61 eV). A more negative E_{ads} corresponds to stronger adsorption. Thus, the adsorption strength of $*NO_3^-$ on the catalyst decreases in the order Fe@Fe_2O_3 > Co-Fe@Fe_2O_3 > Co, indicating that Co-Fe@Fe_2O_3 exhibits a moderate adsorption strength, which is favorable for both adsorption and desorption and could facilitate the NO_3^-RR. Moreover, the

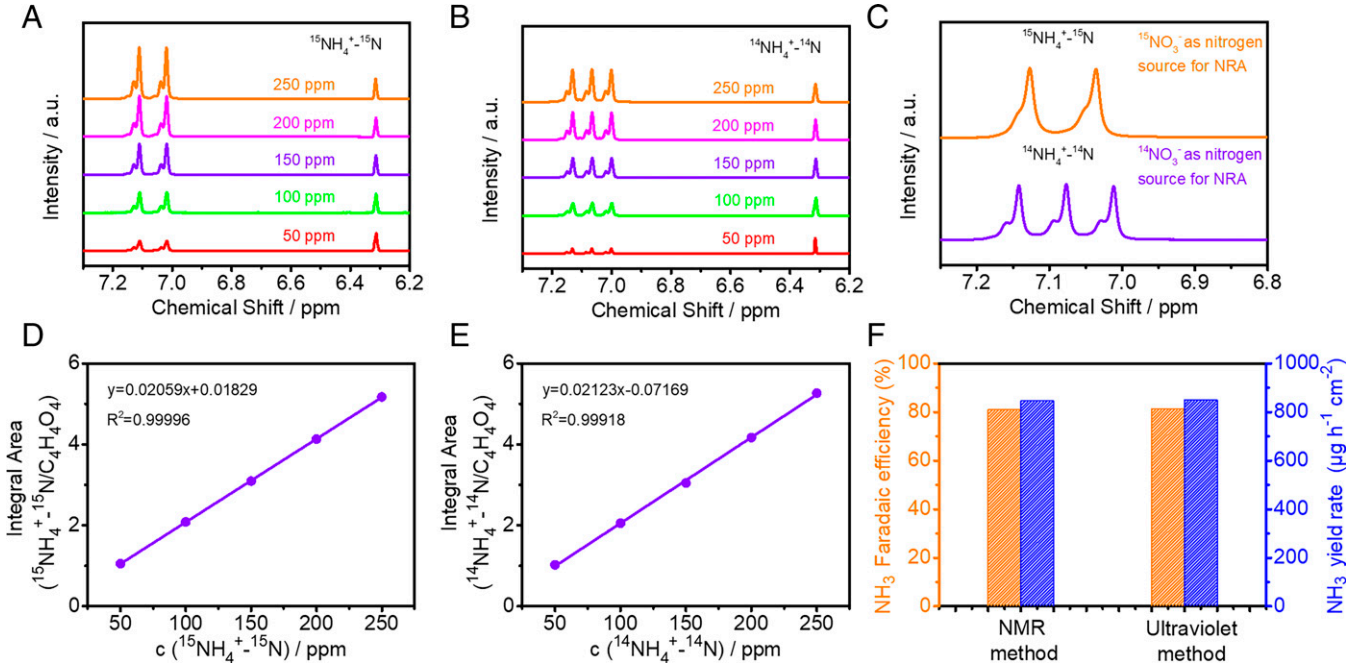

Fig. 5. ^{15}N isotope labeling ^{1}H-NMR spectra (800 MHz). (*A* and *B*) ^{1}H NMR spectra of $^{15}NH_4^+$ and $^{14}NH_4^+$ standard samples of different concentrations. The maleic acid proton appears at δ = 6.31 ppm. The ^{1}H NMR spectra of $^{15}NH_4^+$ contain doublet at δ = 7.10 and 6.98 ppm. The ^{1}H-NMR spectra of $^{14}NH_4^+$ contain triplet at δ = 7.13, 7.05, and 6.96 ppm. (*D* and *E*) Standard curves of integral areas ($^{15}NH_4^+$-^{15}N/$C_4H_4O_4$) and ($^{14}NH_4^+$-^{14}N/$C_4H_4O_4$) against $^{15}NH_4^+$-^{15}N and $^{14}NH_4^+$-^{14}N concentrations, respectively. (*C*) ^{1}H-NMR spectra of the electrolyte after 4 h of NO_3^-RR electrolysis on Co-Fe@Fe_2O_3 using $^{14}NO_3$ and $^{15}NO_3$ as the nitrogen source. (*F*) NH_3 yield rate and FEs determined by ^{1}H-NMR spectroscopy and UV-vis after 4 h.

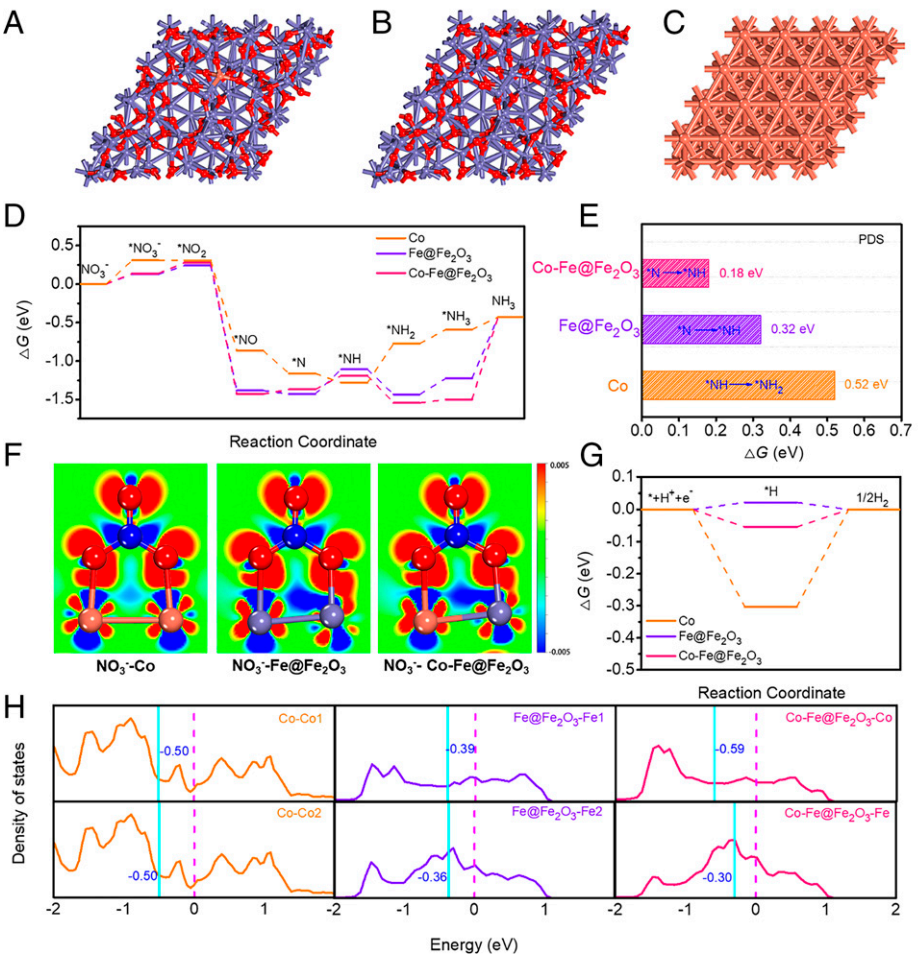

Fig. 6. Mechanistic study of catalytically active sites in Co-Fe@Fe_2O_3 for NO_3^-RR. Optimized structures of (*A*) Co-Fe@Fe_2O_3, (*B*) Fe@Fe_2O_3, and (*C*) Co. Orange, purple, and red spheres represent Co, Fe, and O, respectively. (*D*) Free energy diagram for Co-Fe@Fe_2O_3, Fe@Fe_2O_3, and Co at equilibrium potential. (*E*) PDS energy barriers of Co-Fe@Fe_2O_3, Fe@Fe_2O_3, and Co. (*F*) Electron density of NO_3^- on Co, Fe@Fe_2O_3, and Co-Fe@Fe_2O_3. Orange, violet, blue, and red spheres represent Co, Fe, N, and O atoms, respectively. Blue and red regions indicate electron-donating and electron-withdrawing areas, respectively. (*G*) H_2 formation energies. (*H*) Calculated density of states and d-band centers (the integral domain was set to [−2.0, 2.0 eV]) of the metal active sites of different catalysts. Dashed magenta and solid cyan lines represent the Fermi level and the calculated energy level of the d-band center, respectively (the Fermi level is set at zero energy).

calculations reveal the crucial role of Fe active sites neighboring Co sites (Fe_{Co}) for NO_3^-RR activation.

Next, the electrochemical reaction $NO_3 + 6H_2O + 8e\ NH_3 + 9OH$ was modeled using a series of deoxidation reactions, $*NO_3^- \rightarrow *NO_2^- \rightarrow *NO \rightarrow *N$, followed by hydrogenation reactions, $*N \rightarrow *NH \rightarrow *NH_2 \rightarrow *NH_3$, according to a previous report (52). To illustrate the influence of Co doping on the reaction pathways, we calculated the free energy diagrams for NO_3^- reduction (Fig. 6*D*). The optimized structures of key NO_3^-RR intermediates are shown in *SI Appendix*, Figs. S23–S25. For both Fe@Fe_2O_3 and Co-Fe@Fe_2O_3, the potential-dependent step (PDS) is the reduction of *N to *NH, for which the calculated free energies are 0.32 and 0.18 eV, respectively. For pure Co, the PDS is the reduction of *NH to $*NH_2$, having a free energy of 0.52 eV (Fig. 6*E*). These results suggest that the Co dopant activates adjacent Fe_{Co} active sites, resulting in reduced energy barriers in comparison with those over pristine Fe@Fe_2O_3. Thus, Co and Fe_{Co} synergistically enhance the NO_3^-RR activity of Co-Fe@Fe_2O_3. Therefore, in NO_3^-RR, the main effects of Co doping are 1) being the key NO_3^-RR active sites and 2) being an activator of Fe sites, thus enhancing the intrinsic NO_3^-RR activity of Fe@Fe_2O_3.

The interactions between the three catalysts and NO_3^- were investigated further by calculating the charge densities of the three model systems (Fig. 6*F*). There was charge accumulation (red) around the O atoms and charge depletion (blue) around the Co and Fe atoms. In addition, the electrons from the highest occupied molecular orbital of the NO_3^- molecules transfer to the empty d-orbitals of the Co or Fe centers, resulting in stronger O-Co or O-Fe bonds. Meanwhile, the fully occupied Co or Fe 3d orbital donates electrons to the lowest unoccupied molecular orbital of the NO_3^- molecules, significantly weakening the n = O bonds and facilitating n = O bond cleavage. This implies a charge transfer between NO_3^- and Fe or Co, which is crucial for NO_3^-RR electrocatalysis. Importantly, the Co dopants tune the energy of the d-orbitals of Fe to enhance the charge transfer between Co-Fe@Fe_2O_3 and NO_3^-, thus enhancing performance. In addition, a more significant electron transfer between NO_3^- and Fe_{Co} in Co-Fe@Fe_2O_3 was observed than that between NO_3^- and Fe in Fe@ Fe_2O_3. This result is consistent with the calculated NO_3^- adsorption energies.

To probe the origin of the high performance of Co-Fe@Fe_2O_3, the free energies of the HER on Co-Fe@Fe_2O_3, Fe@Fe_2O_3, and Co NPs were calculated. For the HER, the optimized structures of adsorbed *H are shown in *SI Appendix*, Fig. S26. The free energies for H adsorption (ΔG_{*H}) were calculated to be −0.30, 0.02, and −0.05 eV for Co, Fe@Fe_2O_3,

and Co-Fe@Fe_2O_3, respectively (Fig. 6*G*). Moreover, the ΔG of H_2 formation on the Co surface was calculated to have a higher energy barrier than those on Co-Fe@Fe_2O_3 and Fe@Fe_2O_3, suggesting that Co inhibits HER activity. Thus, although Co has a low nitrate reduction efficiency, it inhibits HER activity, resulting in the high selectivity and FE observed experimentally in Co-Fe@Fe_2O_3.

To gain insight into the different NO_3^-RR activities of the catalysts, the d-band centers (ε_d) of the metal active sites were calculated. As shown in Fig. 6*H*, the calculated ε_d values for the two Co active sites are −0.50 and −0.50 eV; for the two Fe active sites of Fe@Fe_2O_3, the calculated ε_d values are −0.39 and −0.36 eV, indicating the stronger binding of NO_3^- on Fe@Fe_2O_3 than that on Co. Further, with Co doping, the ε_d of the Fe active site shifts to higher energy (−0.30 eV), whereas the ε_d of the Co dopants shifts to lower energy (−0.59 eV); thus, the binding strength of NO_3^- on Co-Fe@Fe_2O_3 is slightly weaker than that on Fe@Fe_2O_3. As shown in *SI Appendix*, Fig. S27, the hybridization between the O atoms of NO_3^- and the Fe_{Co} atom of Co-Fe@Fe_2O_3 is more favorable than that between the O atoms of NO_3^- and Fe atoms of Fe@Fe_2O_3 or Co atoms of Co. Thus, Co doping changes the Fe 3d orbital configuration and enhances the activity of Fe for NO_3^- reduction to NH_3. Therefore, the excellent catalytic NO_3^-RR performance of Co-Fe@Fe_2O_3 can be ascribed to the optimal adsorption strength of the reaction intermediates on Co-Fe@Fe_2O_3.

Conclusions

In summary, we used Co-doped Fe-MOF-74 as a precursor to prepare a Co-doped Fe@Fe_2O_3 catalyst, in which Co replaces some Fe sites in Fe_2O_3. For the NO_3^-RR, Co-Fe@Fe_2O_3 exhibited high catalytic activity and NH_3 selectivity. A mechanistic study further revealed that the high catalytic performance of Co-Fe@Fe_2O_3 can be attributed to the Co dopant, which affects the Fe d orbitals, thereby changing the adsorption energy of the intermediates and free energies of the PDS as well as suppressing the HER. The results of this work suggest that doping an MOF precursor allows the d-band centers of metal-based catalysts to be finely tuned, yielding a high nitrate removal capacity, selectivity, and FE for the NO_3^-RR.

Materials and Methods

Materials. $FeCl_2{\cdot}4H_2O$, and *N*, *N*-dimethylformamide (DMF) were purchased from Sinopharm Chemical Reagent Co., Ltd and used without further purification. $Co(NO_3)_2{\cdot}6H_2O$ and H_4DOBDC were purchased from J&K Chemical Company.

Catalyst Preparation.

Synthesis of Co-MOF-74. Co-MOF was prepared according to the literature method (53) with some modification. Briefly, in a 100-mL beaker, 0.180 g H_4DOBDC, 0.891 g $Co(NO_3)_2{\cdot}6H_2O$, 25 mL H_2O, 25 mL DMF, and 25 mL ethanol were added, ultrasonicated until homogeneous, transferred to a 100-mL Teflon-sealed autoclave, and heated to 100 °C for 24 h. After the solution had cooled to room temperature, the product was collected by centrifugation, washed three times with methanol, and soaked in methanol six times for 3 d. Finally, the product was collected by centrifugation, dried in vacuo at 60 °C, and ground before use.

Synthesis of Fe-MOF-74. Typically, 0.891 g $FeCl_2{\cdot}4H_2O$ was added to 80 mL of a DMF solution of 0.180 g H_4DOBDC. Then, the mixture was transferred to a 100-mL Teflon-sealed autoclave and heated to 110 °C for 12 h. After the solution had cooled to room temperature, the product was collected by centrifugation, washed three times with methanol, and soaked in methanol six times for 3 d. Finally, the product was collected and dried in vacuo at 60 °C.

Synthesis of the Co-doped Fe-MOF-74. Co-doped Fe-MOF-74s (Co-Fe MOFs) were synthesized in the same way as for the Fe-MOF-74, but an additional 10 mg of Co MOF was added to the Fe-MOF-74 precursor solution.

Synthesis of the CoNPs, Fe@Fe_2O_3, and Co-Fe@Fe_2O_3 catalysts. The obtained Co MOF, Fe-MOF, and Co-Fe MOF were placed in a ceramic boat, heated to 900 °C at a ramp rate of 5 °C min^{-1}, and maintained at this temperature for 2 h in a tube furnace under an argon atmosphere. Subsequently, the furnace was allowed to cool to room temperature. Hereafter, these materials are labeled as Co, Fe@Fe_2O_3, and Co-Fe@Fe_2O_3, respectively.

Synthesis of the Co-Fe@Fe_2O_3-t catalysts. Co-Fe@Fe_2O_3-t was synthesized in the same way as Co-Fe@Fe_2O_3. The obtained Co-Fe MOF was pyrolyzed at different temperatures (600 °C, 700 °C, 800 °C, 900 °C, and 1,000 °C) at a ramp rate of 5 °C min^{-1} and maintained at this temperature for 2 h in a tube furnace under an argon atmosphere to form Co-Fe@Fe_2O_3-t (t indicates the pyrolysis temperature).

Material Characterization. Sample morphologies were characterized by scanning electron microscopy using a high-performance field emission scanning electron microscope (Zeiss Merlin). TEM images were collected using a JEOL JEM 2010F fitted with an EDX unit. The chemical composition was investigated using XPS (Escalab 250Xi; Thermo Fisher Scientific) with monochromatic 150-W Al–K_a radiation. The peak positions were calibrated to the C1s peak. The textural properties of the samples were analyzed using an Autosorb-1MP–type N_2-physisorption surface area and porosity analyzer (Quantachrome). The specific surface area was calculated using the BET method from the data in a relative pressure (P/P_0) range of 0.05 to 0.25; pore size distribution plots were derived from the adsorption branch of the isotherms using the Barrett–Joyner–Halenda model. XRD phase analysis was carried on a D/max-B (Rigaku) diffraction and a Cu–K_α source (λ = 0.154056 nm) at a scan rate (2θ) of 1° min^{-1} with an accelerating voltage of 40 kV. UV-vis absorbance spectra were measured using an HACH 6000 spectrophotometer. The isotope-labeled samples were analyzed using an 800-MHz ^{1}H-NMR spectrometer (Bruker).

Electrochemical Analysis of Nitrate Reduction. Measurements were carried out at room temperature using a typical cylindrical three-electrode, one-compartment cell (effective volume = 50 mL). A platinum wire and a saturated calomel electrode (SCE) were used as the counterelectrode and reference electrode, respectively. Nickel foam was coated with the catalyst NPs and used as the working electrode (1.5 × 1.5 cm). The recorded potential was converted to the RHE scale as follows: E (vs. RHE) = E (vs. SCE) + 0.242+ 0.059 pH. The working electrode was prepared using a mixture of catalyst powder (4 mg), acetylene black (0.5 mg), and polyvinylidene difluoride (0.5 mg) dissolved in *N*-methyl-2-pyrrolidone (20 μL), ground to a uniform paste, evenly coated on nickel foam, and dried at 60 °C in a vacuum oven for 12 h. The final working electrode sheet was obtained by pressing the treated nickel foam at 20 MPa. Electrochemical tests were performed on an electrochemical workstation (Ivium Stat) at −0.445 to −0.945 V, and the electrolyte was stirred at 300 rpm. A 1,000-ppm sodium nitrate stock solution was used to prepare 50-mL solutions of various concentrations (50, 200, 500, and 1,000 ppm). The electrolyte was 0.1 M Na_2SO_4. The product concentrations, including nitrite, nitrite, and ammonium, after reaction were analyzed. LSV was used to measure the electrocatalytic activity between voltages of −0.945 and 0.655 V. All potentials were recorded against the RHE.

Ion Concentration and Conversion Efficiency Calculations. A UV-Vis spectrophotometer (DR-6000; Hach Co.) was used to determine the concentrations of nitrate, nitrite, and ammonium. The products after reaction were taken out and diluted to 10 mL to detection range.

Determination of nitrate-N. One molar HCl (0.2 mL) and 0.8 wt % sulfamic acid solution (0.02 mL) were added to the diluted solution described above. The absorption intensities at wavelengths of 220 and 275 nm were recorded. The final absorbance value was calculated by the following equation: $A = A_{220nm} - 2A_{275nm}$. Absolute calibration was achieved by using $NaNO_3$ solutions of the known concentration as standards, and a good linear fit was observed with the absorbance of NO_3^- concentration ($y = 0.24749x - 0.00289$, $R^2 = 0.9998$).

Determination of nitrite-N. *P*-aminobenzenesulfonamide (20 g), *N*-(1-Naphthyl) ethylenediamine dihydrochloride (1 g), ultrapure water (500 mL), and phosphoric acid (50 mL) were mixed as a color reagent. Then, 0.2 mL of this color reagent was added to the diluted solution described above. The absorption intensity at a wavelength of 540 nm was recorded after resting for 20 min. Absolute calibration was achieved by using $NaNO_2$ solutions of the known concentration as standards, and a good linear fit was observed with absorbance and NO_2^- concentration ($y = 3.22336x - 0.00169$, $R^2 = 0.9996$).

Determination of ammonia-N. Potassium sodium tartrate solution (0.2 mL, ρ = 500 g/L) and Nessler's reagent (0.3 mL) were added to the diluted solution described above. The absorption intensity at a wavelength of 420 nm was recorded after resting for 10 min. The standard curve was plotted with the absorbance values on the y axis and the concentration of NH_3 on the x axis. The resulting standard curve ($y = 0.19955x - 0.00002$, $R^2 = 0.9999$) shows a good linear agreement between the absorbance value and NH_3 concentration.

The nitrate removal efficiency was calculated as

$$\text{conversion} = \frac{(C_0 - C_t)}{C_0} \times 100\%,$$

where C_0 (parts per million) represents the initial concentration and C_t (parts per million) is the concentration after the reaction at time t.

The nitrate removal capacity per unit weight of catalyst was calculated as

$$\text{removal capacity} = \frac{(C_0 - C_t)V}{m},$$

where V (liters) is the volume of the nitrate solution and m (grams) is the mass of the catalyst on the nickel foam.

The ammonia and nitrite selectivities were obtained using

$$\text{selectivity} = \frac{C}{(C_0 - C_t)} \times 100\%,$$

where C is the generated concentration of ammonia and nitrite.

The ammonia FE was calculated as

$$\text{faradaic efficiency} = \frac{8F \times C_{NH3} \times V}{M_{NH3} \times Q},$$

where 8 is the number of electron transfers toward the formation of 1 mol of ammonia, F is the Faraday constant (96,485 C mol^{-1}), C is the ammonia concentration, V is the catholyte volume (milliliters), M is the molar mass of NH_3, and Q is the total charge passing through the electrode.

The ammonia production rate (yield) was as

$$\text{yield}_{NH3} = \frac{C_{NH3} \times V}{t \times S},$$

where t is the electrolysis time and S is the geometric area of the working electrode (1.5 × 1.5 cm^2).

The half-cell EE was calculated using the following equation:

$$EE_{NH3} = \frac{(1.23 - E^0_{NH3})FE_{NH3}}{1.23 - E},$$

where E^0_{NH3} is the equilibrium potential (0.70 V) of nitrate electroreduction to ammonia, FE_{NH3} is the FE for NH_3, 1.23 V is the equilibrium potential of water oxidation (i.e., assuming that the overpotential of the water oxidation is zero), and E is the applied potential (vs. RHE) for NH_3 production.

ECSA Evaluation. The ECSA was obtained by measuring the electrochemical double-layer capacitance (C_{dl}) within the potential window without a faradaic response. All catalysts were scanned within the potential range of 0.435 to 0.535 V vs. RHE in 0.1 M $NaSO_4$ at various sweep rates (20 to 160 mV s^{-1}). The current densities at 0.48 V vs. RHE at different sweep rates were then calculated and plotted against the sweep rates for each catalyst. By performing linear fitting, the slopes of the current densities vs. sweep rates were obtained, thus giving the C_{dl} values for the different catalysts. The relationship between the gravimetric C_{dl} (farad $gram^{-1}$) and $I_{capacitive}$ is

$$C_{dl} = \frac{I}{vm},$$

where v is the given scan rate and m is the mass of catalyst on the electrode.

The ECSA was calculated as

$$\text{ECSA} = \frac{C_{dl}}{C_s},$$

where C_s (=0.4 F m^{-2}) is the general specific capacitance for an atomically smooth planar surface under homogeneous electrolytic conditions.

XANES and EXAFS. XANES and EXAFS measurements were performed at the BL14W beamline at the Shanghai Synchrotron Radiation Facility (SSRF) to study the coordination states of Fe and Co. The storage rings of the SSRF were operated at 3.5 GeV with a stable current of 200 mA. Using an Si (111) double-crystal monochromator, data collection was carried out in fluorescence mode using a Lytle detector. All spectra were collected under ambient conditions. Fe foil, Fe_2O_3, Co foil, and CoO were used as the reference samples. The obtained XANES and EXAFS data were analyzed using ATHENA.

DFT Calculations. Spin-polarized calculations were performed using the Vienna ab initio simulation package (54, 55). The ion–electron interactions were described by the projector augmented wave method (56), and the general gradient approximation Perdew–Burke–Ernzerhof functional was used (57, 58). During structure relaxation, the convergence criteria for the residual force and energy were set to 0.03 eV $Å^{-1}$ and 10^{-5} eV, respectively. A 4 × 4 supercell of Co (111) was used as the model for Co; the bottom two layers were fixed, but the top two layers were relaxed. The Fe@Fe_2O_3 model was a 3 × 3 supercell of Fe_2O_3 (001) on a 4 × 4 supercell of Fe (111). Co-Fe@Fe_2O_3 was constructed by substituting one Co atom for one Fe atom on the model surface. Brillouin zones were sampled using 3 × 3 × 1 and 2 × 2 × 1 Monkhorst–Pack k-point grids for Co and Fe@Fe_2O_3/Co-Fe@ Fe_2O_3, respectively. A vacuum space of 15 Å was employed to avoid interactions between two periodic units.

The NO_3^-RR on different catalyst surfaces was simulated according to the following reactions:

$$*NO_3^- + H_2O + e^- \rightarrow *NO_2 + 2OH^-,$$

$$*NO_2 + 2H_2O + 2e^- \rightarrow *NO + 2OH^-,$$

$$*NO + H_2O + 2e^- \rightarrow *N + 2OH^-,$$

$$*N + H_2O + e^- \rightarrow *NH + OH^-,$$

$$*NH + H_2O + e^- \rightarrow *NH_2 + OH^-,$$

$$*NH_2 + H_2O + e^- \rightarrow *NH_3 + OH^-.$$

Here, the asterisk represent an adsorption site.

The free energy change (ΔG) of each elementary reaction was calculated using

$$\Delta G = \Delta E + \Delta E_{ZPE} - T\Delta S,$$

where ΔE, E_{ZPE}, T, and S are the reaction energy difference, zero-point energy, temperature, and entropy, respectively.

Isotope Labeling and ^{1}H-NMR Experiments. Isotope labeling was used to determine the source of the nitrogen in the products. A 98.5% concentration of $Na^{15}NO_3$ was used as the N source during nitrate reduction. The electrolytes for the NO_3^-RR were 0.1 M Na_2SO_4 and 500 ppm $^{15}NO_3^-$-^{15}N.

^{1}H-NMR spectroscopy was used to quantify ammonia and identify its source. A calibration curve was created as follows. First, a series of $^{15}NH_4^+$-^{15}N standard solutions [$(^{15}NH_4)_2SO_4$] having known concentrations (50, 100, 150, 200, 250 ppm) were prepared with 0.1 M Na_2SO_4. Second, 50 mL of the $^{15}NH_4^+$-^{15}N standard solution with different concentrations of external standards (0.02 g maleic acid) was prepared. Third, 50 μL deuterium oxide (D_2O) was added to the mixture (0.45 mL). Finally, a linear relationship between the integrated peak area ratio of $^{15}NH_4^+$-^{15}N and maleic acid and the $^{15}NH_4^+$-^{15}N concentration was obtained. Accordingly, when $Na^{15}NO_3$ and $Na^{14}NO_3$ were used as the N sources, the electrolytes containing $^{15}NH_4^+$-^{15}N and $^{14}NH_4^+$-^{14}N after electrocatalytic reduction for 4 h were removed, the solution was adjusted to a weakly acidic pH with 4 M H_2SO_4, and further quantification was carried out using the above method. The $^{14}NH_4^+$ and $^{15}NH_4^+$ signals can be distinguished because $^{14}NH_4^+$appears as a triplet and $^{15}NH_4^+$ appears as a doublet.

Data Availability. All study data are included in the article and *SI Appendix*.

ACKNOWLEDGMENTS. We acknowledge National Natural Science Foundation of China Grants 41977162 and 52091543 and National Key Research and Development Program Grants 2020YFC1808300 and 2019YFC1806200 for financial support of this work.

1. J. N. Tiwari *et al.*, Multi-heteroatom-doped carbon from waste-yeast biomass for sustained water splitting. *Nat. Sustain.* **3**, 556–563 (2020).
2. Y. Wu, Z. Jiang, Z. Lin, Y. Liang, H. Wang, Direct electrosynthesis of methylamine from carbon dioxide and nitrate. *Nat. Sustain.* **4**, 725–730 (2021).
3. P. Chen *et al.*, Interfacial engineering of cobalt sulfide/graphene hybrids for highly efficient ammonia electrosynthesis. *Proc. Natl. Acad. Sci. U.S.A.* **116**, 6635–6640 (2019).
4. K. Chu *et al.*, Multi-functional Mo-doping in MnO_2 nanoflowers toward efficient and robust electrocatalytic nitrogen fixation. *Appl. Catal. B* **264**, 118525 (2020).
5. S. Z. Andersen *et al.*, A rigorous electrochemical ammonia synthesis protocol with quantitative isotope measurements. *Nature* **570**, 504–508 (2019).
6. Y. Wang, W. Zhou, R. Jia, Y. Yu, B. Zhang, Unveiling the activity origin of a copper-based electrocatalyst for selective nitrate reduction to ammonia. *Angew. Chem. Int. Ed. Engl.* **59**, 5350–5354 (2020).
7. G.-F. Chen *et al.*, Electrochemical reduction of nitrate to ammonia via direct eight-electron transfer using a copper-molecular solid catalyst. *Nat. Energy* **5**, 605–613 (2020).
8. P. Li, Z. Jin, Z. Fang, G. Yu, A single-site iron catalyst with preoccupied active center that achieves selective ammonia electrosynthesis from nitrate. *Energy Environ. Sci.* **1**, 3522–3531 (2021).

9. X. Fu *et al.*, Alternative route for electrochemical ammonia synthesis by reduction of nitrate on copper nanosheets. *Appl. Mater. Today* **19**, 100620 (2020).
10. M. M. Shi *et al.*, Au sub-nanoclusters on TiO_2 toward highly efficient and selective electrocatalyst for N_2 conversion to NH_3 at ambient conditions. *Adv. Mater.* **29**, 1606550 (2017).
11. L. Zhang *et al.*, Electrochemical ammonia synthesis via nitrogen reduction reaction on a MoS_2 catalyst: Theoretical and experimental studies. *Adv. Mater.* **30**, e1800191 (2018).
12. J. M. McEnaney *et al.*, Electrolyte engineering for efficient electrochemical nitrate reduction to ammonia on a titanium electrode. *ACS Sustain. Chem. Eng.* **8**, 2672–2681 (2020).
13. M. Arif *et al.*, Hierarchical hollow nanotubes of NiFeV-layered double hydroxides@CoVP heterostructures towards efficient, pH-universal electrocatalytical nitrogen reduction reaction to ammonia. *Appl. Catal. B* **265**, 118559 (2020).
14. Y. C. Wan, J. C. Xu, R. T. Lv, Heterogeneous electrocatalysts design for nitrogen reduction reaction under ambient conditions. *Mater. Today* **27**, 69–90 (2019).
15. J. Wang *et al.*, Ambient ammonia synthesis via palladium-catalyzed electrohydrogenation of dinitrogen at low overpotential. *Nat. Commun.* **9**, 1795–1801 (2018).
16. D. Bao *et al.*, Electrochemical reduction of N_2 under ambient conditions for artificial N_2 fixation and renewable energy storage using N_2/NH_3 cycle. *Adv. Mater.* **29**, 1604799 (2017).
17. B. H. R. Suryanto *et al.*, Challenges and prospects in the catalysis of electroreduction of nitrogen to ammonia. *Nat. Catal.* **2**, 290–296 (2019).
18. A. R. Singh *et al.*, Electrochemical ammonia synthesis—the selectivity challenge. *ACS Catal.* **7**, 706–709 (2017).
19. J. Gao *et al.*, Non-precious Co_3O_4-TiO_2/Ti cathode based electrocatalytic nitrate reduction: Preparation, performance and mechanism. *Appl. Catal. B* **254**, 391–402 (2019).
20. S. Garcia-Segura, M. Lanzarini-Lopes, K. Hristovski, P. Westerhoff, Electrocatalytic reduction of nitrate: Fundamentals to full-scale water treatment applications. *Appl. Catal. B* **236**, 546–568 (2018).
21. L. Su *et al.*, Tailoring the assembly of iron nanoparticles in carbon microspheres toward high-performance electrocatalytic denitrification. *Nano Lett.* **19**, 5423–5430 (2019).
22. J. Gao, B. Jiang, C. Ni, Y. Qi, X. Bi, Enhanced reduction of nitrate by noble metal-free electrocatalysis on P doped three-dimensional Co_3O_4 cathode: Mechanism exploration from both experimental and DFT studies. *Chem. Eng. J.* **382**, 123034 (2020).
23. W. Qu *et al.*, Single-atom catalysts reveal the dinuclear characteristic of active sites in NO selective reduction with NH_3. *Nat. Commun.* **11**, 1532–1538 (2020).
24. J.-X. Liu, D. Richards, N. Singh, B. R. Goldsmith, Activity and selectivity trends in electrocatalytic nitrate reduction on transition metals. *ACS Catal.* **9**, 7052–7064 (2019).
25. Y. Yu, C. Wang, Y. Yu, Y. Wang, B. Zhang, Promoting selective electroreduction of nitrates to ammonia over electron-deficient Co modulated by rectifying Schottky contacts. *Sci. China Chem.* **63**, 1469–1476 (2020).
26. J. Li *et al.*, Efficient ammonia electrosynthesis from nitrate on strained ruthenium nanoclusters. *J. Am. Chem. Soc.* **142**, 7036–7046 (2020).
27. E. Pérez-Gallent, M. C. Figueiredo, I. Katsounaros, M. T. M. Koper, Electrocatalytic reduction of nitrate on copper single crystals in acidic and alkaline solutions. *Electrochim. Acta* **227**, 77–84 (2017).
28. Y. Lan, J. Chen, H. Zhang, W.-x. Zhang, J. Yang, Fe/Fe_3C nanoparticle-decorated N-doped carbon nanofibers for improving the nitrogen selectivity of electrocatalytic nitrate reduction. *J. Mater. Chem. A Mater.* **8**, 15853–15863 (2020).
29. W. Ye *et al.*, Precisely tuning the number of Fe atoms in clusters on N-doped carbon toward acidic oxygen reduction reaction. *Chem* **5**, 2865–2878 (2019).
30. W. Teng *et al.*, Selective nitrate reduction to dinitrogen by electrocatalysis on nanoscale iron encapsulated in mesoporous carbon. *Environ. Sci. Technol.* **52**, 230–236 (2018).
31. Y. Wan *et al.*, Oxidation state modulation of bismuth for efficient electrocatalytic nitrogen reduction to ammonia. *Adv. Funct. Mater.* **31**, 2100300 (2021).
32. H. F. Wang, L. Chen, H. Pang, S. Kaskel, Q. Xu, MOF-derived electrocatalysts for oxygen reduction, oxygen evolution and hydrogen evolution reactions. *Chem. Soc. Rev.* **49**, 1414–1448 (2020).
33. S. Wang, C. M. McGuirk, A. d'Aquino, J. A. Mason, C. A. Mirkin, Metal-organic framework nanoparticles. *Adv. Mater.* **30**, e1800202 (2018).
34. H. B. Wu, X. W. D. Lou, Metal-organic frameworks and their derived materials for electrochemical energy storage and conversion: Promises and challenges. *Sci. Adv.* **3**, eaap9252 (2017).
35. A. Mahmood, W. Guo, H. Tabassum, R. Zou, Metal-organic framework-based nanomaterials for electrocatalysis. *Adv. Energy Mater.* **6**, 1600423 (2016).
36. R. V. Jagadeesh *et al.*, MOF-derived cobalt nanoparticles catalyze a general synthesis of amines. *Science* **358**, 326–332 (2017).
37. S. Zhang *et al.*, Highly stable supercapacitors with MOF-derived Co_9S_8/carbon electrodes for high rate electrochemical energy storage. *J. Mater. Chem. A Mater.* **5**, 12453–12461 (2017).
38. X. Wang *et al.*, Strategies for design of electrocatalysts for hydrogen evolution under alkaline conditions. *Mater. Today* **36**, 125–138 (2020).
39. P. H. Chung *et al.*, A sensitive visible light photodetector using cobalt-doped zinc ferrite oxide thin films. *ACS Appl. Mater. Interfaces* **13**, 6411–6420 (2021).
40. Z. Ji *et al.*, High energy density hybrid supercapacitor based on cobalt-doped nickel sulfide flower-like hierarchitectures deposited with nitrogen-doped carbon dots. *Nanoscale* **13**, 1689–1695 (2021).
41. J. Lim, Y. Yang, M. R. Hoffmann, Activation of peroxymonosulfate by oxygen vacancies-enriched cobalt-doped black TiO_2 nanotubes for the removal of organic pollutants. *Environ. Sci. Technol.* **53**, 6972–6980 (2019).
42. H.-W. Man *et al.*, Transition metal-doped nickel phosphide nanoparticles as electro- and photocatalysts for hydrogen generation reactions. *Appl. Catal. B* **242**, 186–193 (2019).
43. H. Li *et al.*, Hollow shell-in-shell Ni_3S_4@Co_9S_8 tubes derived from core–shell Ni-MOF-74@Co-MOF-74 as efficient faradaic electrodes. *CrystEngComm* **20**, 889–895 (2018).
44. L. Zhang *et al.*, Air cathode of zinc-air batteries: A highly efficient and durable aerogel catalyst for oxygen reduction. *Nanoscale* **11**, 826–832 (2019).
45. D. H. Li *et al.*, Simple pyrolysis of cobalt alginate fibres into Co_3O_4/C nano/microstructures for a high-performance lithium ion battery anode. *J. Mater. Chem. A Mater.* **2**, 18761–18766 (2014).
46. J. Yang, W. Li, D. Wang, Y. Li, Electronic metal-support interaction of single-atom catalysts and applications in electrocatalysis. *Adv. Mater.* **32**, e2003300 (2020).
47. S. Zhang *et al.*, Electrocatalytically active Fe-$(O\text{-}C_2)_4$ single-atom sites for efficient reduction of nitrogen to ammonia. *Angew. Chem. Int. Ed. Engl.* **59**, 13423–13429 (2020).
48. L. Zhang *et al.*, Scalable and controllable synthesis of atomic metal electrocatalysts assisted by an egg-box in alginate. *J. Mater. Chem. A Mater.* **6**, 18417–18425 (2018).
49. W. Zhu *et al.*, Enhanced CO_2 electroreduction on neighboring Zn/Co monomers by electronic effect. *Angew. Chem. Int. Ed. Engl.* **59**, 12664–12668 (2020).
50. Z. Li *et al.*, Directed growth of metal-organic frameworks and their derived carbon-based network for efficient electrocatalytic oxygen reduction. *Adv. Mater.* **28**, 2337–2344 (2016).
51. S. You *et al.*, Enhanced cathodic oxygen reduction and power production of microbial fuel cell based on noble-metal-free electrocatalyst derived from metal-organic frameworks. *Adv. Energy Mater.* **6**, 1501497 (2016).
52. Y. Wang *et al.*, Enhanced nitrate-to-ammonia activity on copper-nickel alloys via tuning of intermediate adsorption. *J. Am. Chem. Soc.* **142**, 5702–5708 (2020).
53. S. R. Caskey, A. G. Wong-Foy, A. J. Matzger, Dramatic tuning of carbon dioxide uptake via metal substitution in a coordination polymer with cylindrical pores. *J. Am. Chem. Soc.* **130**, 10870–10871 (2008).
54. G. Kresse, J. Furthmüller, Efficient iterative schemes for ab initio total-energy calculations using a plane-wave basis set. *Phys. Rev. B Condens. Matter* **54**, 11169–11186 (1996).
55. G. Kresse, D. Joubert, From ultrasoft pseudopotentials to the projector augmented-wave method. *Phys. Rev. B Condens. Matter Mater. Phys.* **59**, 1758–1775 (1999).
56. P. E. Blöchl, Projector augmented-wave method. *Phys. Rev. B Condens. Matter* **50**, 17953–17979 (1994).
57. J. P. Perdew *et al.*, Atoms, molecules, solids, and surfaces: Applications of the generalized gradient approximation for exchange and correlation. *Phys. Rev. B Condens. Matter* **46**, 6671–6687 (1992).
58. J. P. Perdew, Y. Wang, Accurate and simple analytic representation of the electron-gas correlation energy. *Phys. Rev. B Condens. Matter* **45**, 13244–13249 (1992).